IOP Publishing 2D Mater. 0 (2024) xxxxxx https://doi.org/10.1088/2053-1583/ad42ae

2D Materials

PAPER

RECEIVED
14 March 2024

REVISED
8 April 2024

ACCEPTED FOR PUBLICATION
24 April 2024

PUBLISHED
xx xx xxxx

Tuning the water interlayer spacer of microwave-synthesized holey graphene films towards high performance supercapacitor application

Kun Bi[1], Xinyu Jiang[1], Haofan Sun[1], Yan Dou[1], Richard Nile[1], Dini Wang[1], Fazlay Rubbi[2], Xing Zhang[2], Yan Wang[3], Yiliang Liao[2], Kailong Jin[1], Houlong Zhuang[1], Wonmo Kang[1] and Qiong Nian[1,*]

[1] School of Engineering for Matter, Transport and Energy, Arizona State University, Tempe, AZ, United States of America
[2] Department of Industrial & Manufacturing Systems Engineering, Iowa State University, Ames, IA, United States of America
[3] Department of Mechanical Engineering, University of Nevada, Reno, NV, United States of America
[*] Author to whom any correspondence should be addressed.

E-mail: Qiong.Nian@asu.edu

Keywords: holey graphene, supercapacitor, ion diffusion

Supplementary material for this article is available online

Abstract

Graphene-based electrodes have been extensively investigated for supercapacitor applications. However, their ion diffusion efficiency is often hindered by the graphene restacking phenomenon. Even though holey graphene (hG) is fabricated to address this issue by providing ion transport channels, those channels could still be blocked by densely stacked graphene nanosheets. To tackle this challenge, this research aims at improving the ion diffusion efficiency of microwave-synthesized hG films by tuning the water interlayer spacer towards the improved supercapacitor performance. By controlling the vacuum filtration during graphene-based electrode fabrication, we obtain dry films with dense packing and wet films with sparse packing. The SEM images reveal that 20 times larger interlayer distance is constructed in the wet film compared to that in the dry counterpart. The hG wet film delivers a specific capacitance of 239 F g^{-1}, ~82% enhancement over the dry film (131 F g^{-1}). By an integrated experimental and computational study, we quantitatively show that the interlayer spacing in combination with the nanoholes in the basal plane dominates the ion diffusion rate in hG-based electrodes. Our study concludes that novel hierarchical structures should be further considered even in hG thin films to fully exploit the superior advantages of graphene-based supercapacitors.

1. Introduction

In recent years, supercapacitors have drawn extensive attention as potential energy storage devices and power sources for a wide range of applications, including consumer electronics [1], grid power buffer [2], energy harvesting [3], medical devices [4], transportation [5], and more. Supercapacitors typically consist of two electrodes sandwiching one ion-exchange separator, while all these components are immersed in electrolyte solution. When supercapacitors are charged, electrical energy can be stored by separating electrolyte ions and forming the Helmholtz double layer [6]. The performance of supercapacitors strongly depends on three factors: the velocity of electrolyte ion moving within the device, the rate of ion-electron charge transfer at the electrode interface, and the number of ions absorbed on the electrode. Thus, ideal electrode materials should have properties favoring these processes, such as high electrical conductivity [7], high ion mobility [8], good electrochemical activity and large ion-accessible surface area [9].

Graphene has emerged as a potential candidate electrode material because of its high electrical conductivity (10^4–10^5 S m^{-1}) [10], superior electrochemical activity [11] and large specific surface area (2630 m^2 g^{-1}) [12]. To date, graphene-based supercapacitors have demonstrated great electrochemical performance [13–15]. However, further

development of graphene-based supercapacitors is limited by an intrinsic issue: graphene restacking. Specifically, graphene flakes tend to stack together [16] when they are fabricated into electrodes, blocking the transportation of ions and molecules and thereby leading to sluggish diffusion kinetics [17]. This could be even worse when graphene is densely assembled [16] to maximize volumetric energy storage capacity. Therefore, how to accelerate ion diffusion in graphene electrodes becomes a key. To address this issue, previous studies have proposed creating nanoholes on the graphene basal plane to improve the ion diffusion [18–20]. The resulting material, named holey graphene (hG), can facilitate ions travelling through the electrodes with abundant mass transport channels [21] provided by the nanoholes. In addition, the carbon atoms around the nanoholes become electrochemically active edge sites [22, 23]. As a result, hG-based supercapacitors achieved ultrahigh specific capacitance of 298 F g^{-1} [17, 18], representing an improvement of 50% compared to intact graphene-based counterparts. As increasing specific capacitance is reported in research, it is important to develop synthesis processes to manufacture hG at scale.

In a prior study [24], our group developed a scalable hG synthesis method using hydrogen peroxide (H_2O_2) to etch graphene oxide (GO) under microwave, which reduces the processing time from hour-scale to minute-scale. Following the same method, we selected the optimized etching condition to manufacture pure hG-based supercapacitors. However, the restacking of hG flakes is still a critical issue in our hG-based supercapacitor which hinders the further improvement of its performance. This agrees with existing research that only when 3D hierarchical structure in hG electrode is constructed and interlayer spacing is introduced, higher capacitive performance can be obtained. For example, hG-based composite [25], aerogel [26], hydrogel [27], 3D network [28] and framework [17], fiber [29], etc, have been studied recently, demonstrating superior energy storage capability.

In this study, to further reveal the impact of the interlayer spacing on hG-based supercapacitors, we have fabricated hG electrodes with a simple and controllable 3D structure. By controlling the vacuum filtration process, we obtain hG dry films with a small interlayer distance, and wet films with a large interlayer distance using water residue as the interlayer spacer. Studying their performance side-by-side, the hG wet film delivers a specific capacitance of 239 F g^{-1}, about 82% enhancement compared to hG dry film of 131 F g^{-1} due to the enlarged interlayer spacing. In addition to the interlayer spacing, nanoholes on the basal plane of hG flakes also contribute to significant performance enhancement, e.g. a 98% capacitance increase of hG wet film over the rGO wet film without nanoholes. Therefore, our study confirmed that nanoholes and interlayer spacing have a synergetic effect on improving the performance of hG-based supercapacitors. We quantify the impact of each factor, through experimental measurements and density functional theory (DFT) calculations.

2. Experimental section

2.1. Fabrication of holey graphene

The full details of hG preparation can be found in our previous work [24]. The GO water dispersion (GO, 0.4 wt%) is a product of Graphenea. All other chemicals are purchased from Sigma-Aldrich. Briefly, to prepare hG, 1 mg ml^{-1} GO solution (6 ml) was etched in a microwave reactor (Anton Paar Monowave 400, 2.45 GHz) at a constant power of 50 W for 180 s. After cooling, 0.75 ml H_2O_2 (30%) was added, followed by another microwave etching at 50 W for 180 s. The resulting holey graphene oxide (hGO) solution was centrifuged at 12 000 rpm for 30 min and the precipitation was re-dispersed to form hGO aqueous solution, at a concentration of 0.25 mg/mL. Next, to reduce hGO, 24 ml solution was mixed homogeneously with 20 μl hydrazine solution (N_2H_4, 35 wt% in water) and 80 μl of ammonia solution (NH_3, 28 wt% in water), then it was put into a water bath (∼90 °C) for 1 h. The hydrothermal reduction method refers to this prior work[30]. After reduction, reduced holey GO (rhGO) solution is obtained. The control group reduced GO (rGO) solution, was also prepared without etching process but the same hydrothermal treatment.

2.2. Preparation of holey graphene thin film

The thin film is prepared by vacuum filtration from 10 ml rhGO solution through a cellulose filter (0.45 μm pore size, 15 mm; Whatman). The diameter of the round-shape film is around 15 mm. On the one hand, the dry film was prepared by complete vacuum filtration without visible water remaining, then the paper-like dry film was kept in air. The average mass of a dry film is around 1 mg, so the mass loading of rhGO electrode is 0.565 mg cm^{-2}. On the other hand, to prepare the wet film, the vacuum filtration process was controlled to leave a certain amount of residual water in the film. Then the resulting hydrogel-like film was immersed in 1 M H_2SO_4 for ion exchange, since the H_2SO_4 was used as the electrolyte for supercapacitors herein. In addition to dry film and wet film, freeze-dry (FD) film was also prepared for comparison. To prepare a FD film, a wet film is freeze-dried for 24 h by Millrock Technology BT-48 Freeze Dryer. The FD film is kept in air.

2.3. Electrochemical measurements

The electrochemical tests were carried out on a CH Instruments 660 E workstation in ambient condition. The two-electrode assembly setup included two titanium (Grade 2 Titanium Shim Stock, 0.005” thick;

McMaster-Carr) electrodes and a cellulose filter (also used during vacuum filtration) as the membrane. After being immersed in the electrolyte solution (1M H_2SO_4) overnight for ion exchange, a pair of rhGO films (dry, wet or FD) were loading into this setup, separated by the membrane.

The scan windows of both cyclic voltammetry (CV) and galvanostatic charge/discharge (GCD) measurements were 0 V to 1 V. The equations to calculate specific capacitance C_s:

$$C_S = \frac{2I\Delta t}{m\Delta V}\,(\mathrm{GCD})$$

$$C_S = \frac{\int iv\mathrm{d}v}{\mu m\Delta V}\,(\mathrm{CV})\,.$$

GCD: where I is the constant current, m is the mass of the active material, ΔV is the voltage range, and Δt is the time duration of discharge. CV: where i is the instant current, v is the voltage, m is the mass of the active material, ΔV is the voltage range, and μ is the scan rate.

Electrochemical impedance spectroscopy (EIS) was performed at the open-circuit voltage from 1 MHz to 1 Hz.

2.4. Characterization

The morphology of rhGO nanosheet was characterized by transmission electron microscope (TEM, FEI Titan, 300/80) at 300 kV. The chemical information of rhGO was characterized by x-ray Photoelectron Spectroscopy (XPS, Krator Axis Supra +). The Raman data were collected using a 150 mW Coherent Sapphire SF laser with a 532 nm laser wavelength. The morphology of rhGO thin film was characterized by field emission scanning electron microscope (SEM, Zeiss Auriga) and FEI Quanta-FEG 250 field-emission SEM at 10 kV.

2.5. Diffusion model

To calculate the energy barrier for hydrogen ion diffusion and evaluate the effects of interlayer distance on it, we considered two diffusion modes for a hydrogen ion moving between two hG layers with 176 carbon atoms in total: moving from the center of one nanohole to the center of the other nanohole and moving horizontally in the middle plane between two hG layers. We studied three distances for each mode: 7.4 Å, 11.1 Å, and 14.8 Å. The Vienna *Ab initio* Simulation Package (VASP) [31, 32] was applied with the exchange-correlation functional under the generalized gradient approximation and parameterized by Perdew, Burke, and Ernzerhof [33]. We also used a cutoff energy of 550 eV and the projector augmented wave potentials [34]. Furthermore, the climbing image method [35] modified from the nudged elastic band and dispersion correction with Becke–Johnson damping function [36] in VASP were utilized to obtain the energy barrier and minimum energy path (MEP).

3. Results and discussion

3.1. Fabrication of holey graphene

To fabricate hG at scale we employ the method previously reported by our group (the mechanisms are illustrated in figure 1(a). More details in experimental section). This method uses a two-step microwave process including pretreatment and etching. The first step is pretreatment, during which GO flakes are exposed to incident microwave radiation at a constant power. The microwave radiation initiates intense dipole vibration of oxygen-containing functional groups on GO basal plane. As intensive dipole vibration proceeds, those relatively weak chemical bonds will break, so that functional groups and adjacent atoms on GO are partially removed from the lattice, leaving vacancies *in situ*. As a result, pretreatment significantly introduces defects into GO lattice. The second step is etching, during which hydrogen peroxide (H_2O_2) is added, then the solution is again exposed to microwave at a constant power. Under microwave radiation, the H_2O_2 molecules interact with GO sheets and remove carbon atoms, especially those edge-site atoms around vacancies as they are more chemically active. As this etching reaction repeats, the repeating removal of carbon atoms eventually generates nanoholes on GO basal plane. The high efficiency of our hG manufacturing method is attributed to the *in-situ* heating generated by microwave radiation. To be specific, the energy of microwave directly acts on GO-etchant interface, activating violent movement of dipoles and electrons and interaction between GO and H_2O_2 molecules, thus promoting etching reaction. We have also studied the selective heating effect of microwave (supporting materials, figure S1). More details about the manufacturing process and mechanisms can be found in our prior study[37]. Note that although the method used herein is relying on a lab-scale microwave reactor, this process can be potentially scale-up for mass production through specifically designed microwave instruments with continuous processing capability [38–40].

To characterize the morphology of our hG, we use TEM to reveal the evolution from graphene (figure 1(b)) to hG (figure 1(c)). The hG shows multiple nanoholes of 10–30 nm size on the nanoflake, while no nanohole can be found on the graphene in our TEM image. Besides, the surface of graphene flake appears flattened with grey strips formed due to the flake stacking onto thicker sections. However, the surface of hG flake is relatively rugged. These TEM images confirm that hG is successfully fabricated through our manufacturing method.

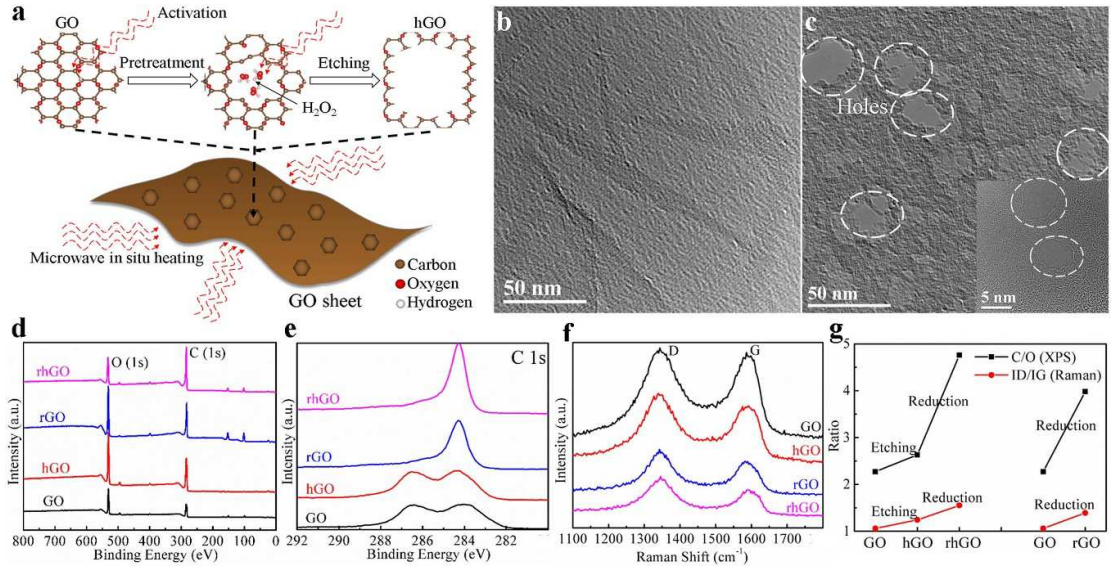

Figure 1. (a) The schematic diagram of holey graphene manufacturing process. The TEM images of (b) graphene and (c) holey graphene with a high-resolution inset. The XPS spectra of (d) survey scan and (e) high resolution spectra of carbon 1 s. (f) Raman spectra showing D band and G band. (g) The carbon/oxygen atomic ratio from XPS data, and I_D/I_G intensity ratio from Raman data. Here, reduced holey graphene oxide (rhGO) can be considered as holey graphene and reduced graphene oxide (rGO, control group) can be considered as graphene.

The XPS spectra present the elemental content and chemical bonding information of GO, hGO, rhGO and rGO. First of all, the survey scan results (figure 1(d)) reveal that the major components are C and O with 1 s peak at 284 eV and 532 eV, respectively. Furthermore, by peak fitting we calculate that the initial material GO has the lowest C/O atomic ratio of 2.27:1, containing most oxygen atoms. After pretreatment and etching process, hGO has a higher ratio of 2.63:1, suggesting partial removal of oxygen atoms and possible formation of nanoholes. We can also infer that the microwave radiation intensively interacts with those oxygen-containing groups or atoms near oxygen, so oxygen atoms are preferentially removed. After following the reduction process, rhGO has the highest ratio of 4.76:1, containing least oxygen atoms. This suggests further removal of oxygen atoms, which agrees with the mechanisms for GO reduction [41]. For comparison, rGO has a ratio of 3.98:1, which is much higher than GO but lower than rhGO. This comparison again verifies the oxygen-removal effect of pretreatment and etching. In addition, the high-resolution XPS spectra of C 1 s region (figure 1(e)) reveal that C–O bonds with binding energy at 287 eV are clearly present in GO and hGO. However, the signal of C–O bond almost disappears after reduction, while the C–C bond signal at 284 eV remains for rGO and rhGO. The significant decrease of C–O bond indicates that oxygen-containing groups are greatly removed, which agrees with the results of survey scan. In conclusion, the increasing C/O ratio from GO to rhGO confirms that the pretreatment and etching process create nanoholes on GO sheets by removing oxygen-containing groups preferentially, then the reduction process further removes oxygen atoms to reduce hGO into rhGO.

The Raman spectra in figure 1(f) present vibrational modes of GO, hGO, rhGO and rGO. The intensity ratio (I_D/I_G) of D band (centered at 1333 cm^{-1}) to G band (centered at 1593 cm^{-1}) is calculated, which indicates the degree of disorder[42]. Initially GO has the lowest I_D/I_G ratio of 1.06:1, suggesting low density of defect on GO basal plane. After pretreatment and etching process, hGO has a higher ratio of 1.24:1, suggesting small number of defects are introduced onto GO. As mentioned earlier, these defects primarily result from the removal of oxygen-contain groups and adjacent atoms on GO. After reduction, rhGO has the highest ratio of 1.55:1, suggesting high degree of disorder and high density of defects. This increasing trend of I_D/I_G indicates further removal of atoms on GO thus *in-situ* vacancies, consistent with the results of XPS. As the control group, rGO has a ratio of 1.39:1, higher than GO but lower than rhGO. Other than D peak and G peak, the 2D peak in these spectra becomes weaker after processing, suggesting stacking of graphene flakes and formation of multilayer aggregation. In conclusion, both etching and reduction process will remove atoms from GO, distort the lattice and leave vacancies *in situ* with dangling bonds, therefore increasing the degree of disorder. This agrees with the conclusion from XPS results. The trend of the C/O atomic ratio and I_D/I_G intensity ratio are summarized as figure 1(g). Similar Raman results were also reported in prior

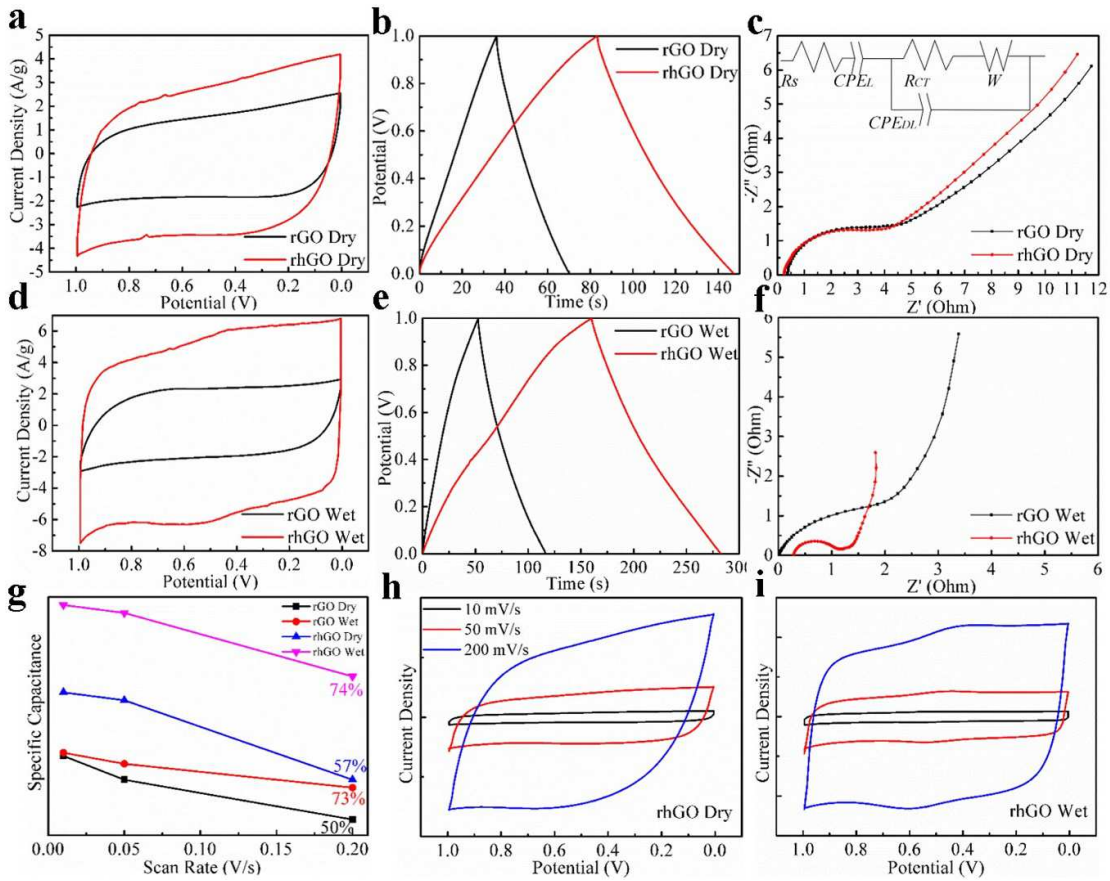

Figure 2. The electrochemical measurements of holey graphene dry film (a)–(c) and wet film (d)–(f). The film is prepared by complete vacuum filtration (dry film) or controlled vacuum filtration (wet film). (a), (d) CV curves at a scan rate of 50 mV s^{-1}, scan window from 1 V to 0 V. (b), (e) GCD curves at a current density of 1 A g^{-1}. (c), (f) Nyquist plot, frequency range from 0.1 Hz to 100 kHz. The inset is the equivalent circuit, Randles circuit. (g)–(i) The performance decay under different scan rate in CV. The electrolyte is 1 M H_2SO_4.

works [19, 24, 43]. Combining the characterization results of TEM, XPS and Raman, the effects of our hG manufacturing method is proven effective.

3.2. Electrochemical measurements

To evaluate the performance of our hG films in supercapacitors, we carried out electrochemical measurements, results shown in figure 2. For the dry film (figures 2(a)–(c)), the CV curves (figure 2(a)) of hG and G are similar in shape, while the parallelogram of hG has a larger loop area. Because the enclosed area of the CV curve is proportional to the capacitance, clearly hG film has a larger specific capacitance. The GCD curves (figure 2(b)) reveal a significant increase of discharging time for hG film, thus a significant increase of capacitance over graphene film. The specific capacitance of hG dry film is calculated to be 131 F g^{-1}, about 79% of enhancement compared to the G control group, 73 F g^{-1}. To study the kinetic process of ion diffusion in the hG supercapacitor during charge and discharge, Nyquist plots (figure 2(c)) are obtained from EIS measurements. In the high frequency region, the radius of the semicircle is proportional to the charge transfer resistance (R_{CT}) at the electrode/electrolyte interface. And in the low frequency region, the slope of the approximate linear section is inversely proportional to the Warburg resistance (W), which determines the bulk diffusion rate. By extrapolating the linear section of the plots to the real axis, both graphene film and hG film show a similar R_{CT} around 4.5 Ω, which suggests similar charge transfer rate at the interface. However, the plot of hG has a larger slope in the low frequency region, indicating lower W, namely, larger ion diffusivity. The inset in figure 2(c) is the modified Randles [44] equivalent circuit, consisting of equivalent series resistance (R_S), R_{CT}, a constant phase element due to the limit capacitance (CPE_L), another constant phase element due to the double-layer capacitance (CPE_{DL}), and Warburg impedance. Following the same method (details in supporting materials) in our previous study [24], we calculate that the diffusivity in hG film is 8.86 × 10^{-12} cm^2 s^{-1}, slightly larger than the value in control group 7.79 × 10^{-12} cm^2 s^{-1}. Comparing the diffusivity, we find out that although the ion diffusion rate increases with the presence of nanoholes, the increase in dry films is not as much as we expected.

Table 1. The specific capacitance of graphene/holey graphene dry/wet film and corresponding improvement resulting from pores in holey graphene or/and interlayer spacing in wet film.

	Dry Film	Wet Film	↑% by Spacing
rGO	73 F g^{-1}	121 F g^{-1}	66%
rhGO	131 F g^{-1}	239 F g^{-1}	82%
↑% by Pore	79%	98%	227% (combined)

Next, we tested the wet film and obtained comparable results (figures 2(d)–(f)). Similar trends are found in CV curves, GCD curves and Nyquist plots. In specific, the CV curves (figure 2(d)) of hG almost has a rectangle shape, with a much larger enclosed area compared to the control group. The GCD curves (figure 2(e)) show sharply increasing discharging time for hG film. As a result, the specific capacitance of hG wet film is calculated to be 239 F g^{-1}, about 98% enhancement compared to 121 F g^{-1} from the control group. Moreover, comparing hG wet film to hG dry film, there is also an enhancement of 82% (239:131, F g^{-1}). The values of specific capacitance and corresponding improvement rate resulting from pores in hG or spacing in wet film are summarized in table 1. The Nyquist plots (figure 2(f)) indicate that hG film has a R_{CT} of 1.0 Ω, only 30% compared to 3.5 Ω from the control group, so the hG film has a much faster charge transfer rate at the electrode/electrolyte interface. This improvement is attributed to nanoholes that form the additional ion-transport channels, and these channels could be more effective when immersed in water. In addition, the plot of hG also has a larger slope in the low frequency region, thus resulting in larger ion diffusivity. The diffusivity in hG wet film is calculated to be 1.33×10^{-9} cm^2 s^{-1}, which is two orders of magnitude higher than that in graphene wet film (7.77×10^{-11} cm^2 s^{-1}), and three orders of magnitude higher than that in dry film ($\sim 8 \times 10^{-12}$ cm^2 s^{-1}). In summary, the specific capacitance and ion diffusivity benefit from two factors simultaneously: nanoholes in hG and water-filled wet film.

Furthermore, we summarize some recent progress in hG-based supercapacitors in table 2. In comparison to hG supercapacitors constructed by mixed slurry pasted on current collector [45] or rod-coating layer [46] on current collectors (no evident interlayer spacer present), our hG wet films exhibit better capacitive performance. However, when compared to those supercapacitors with assembled 3D structures, e.g. nanofiber composite prepared by vacuum filtering [47], GO/cellulose nanofiber films prepared by filtering [48], or chitosan/GO hybrid hydrogel prepared by hydrothermal method [49], our hG wet films exhibit deficient performance. But it is noteworthy that the fabrication process for our hG wet

Table 2. Comparing the electrode structure, electrochemical performance and processing time to fabricate hG (key steps only) between our hG thin films and other supercapacitors recently reported.

Electrode structure	Specific capacitance C_s (F g^{-1})	Energy density (Wh kg^{-1})	Processing time from GO to hG
hG wet film	**239**	**33.2**	**6 min + 1 h**
hG paste [45]	231.4	22	2 h + 12 h
hG coating [46]	111.1	NA	30 min + 1 h
Composite network [47]	237.9	45	4 h + 8 h
hG/cellulose nanofiber film [48]	323	NA	4.5 h
Hybrid hydrogel [49]	377	31	4 h

films is relatively time-efficient and cost-efficient. Meanwhile, the all-carbon electrodes could render long-term stability for multiple charging cycles. More studies on hG-based supercapacitors can be found in our review paper [50] for comparison.

In conclusion, hG film shows significant improvements in electrochemical performance over graphene film. However, the improvement of dry film is not as much as that of wet film. This result suggests that the restacking issue still occurs in hG electrode. One proof is that the specific capacitance of hG could be as low as 61 F g^{-1} when mass loading is high[51]. To further verify the effects of water in wet film, we measured the capacitive performance under different scan rate (figures 2(g)–(i)). Figure 2(g) shows the specific capacitance of rGO dry/wet film and rhGO dry/wet film at scan rates of 0.01 V s^{-1}, 0.05 V s^{-1} and 0.2 V s^{-1}, respectively. Although all four curves exhibit a decreasing trend as the scan rate increases, the two curves of rGO wet film and rhGO wet film decay slowly, retaining 73% and 74% of specific capacitance, respectively. Meanwhile, the rGO dry film and rhGO dry film only retain 50% and 57% of specific capacitance, respectively. The corresponding CV curves (figures 2(h)–(i)) at scan rate of 0.01 V s^{-1} are close to ideal rectangle shape. As scan rate increases, the CV curves of rhGO dry film (figure 2(g)) become skewed, while the curves of wet film (figure 2(i)) approximately maintain the rectangle shape. The slower performance decay of wet film is attributed to the faster ion diffusion in the electrodes filled with water solution. Therefore, wet films have better overall electrochemical performance over dry films.

3.3. Dry film and wet film

To explain the improvements for hG wet film and understand the effects of water, we hypothesize that the residual water acts as spacer to increase the

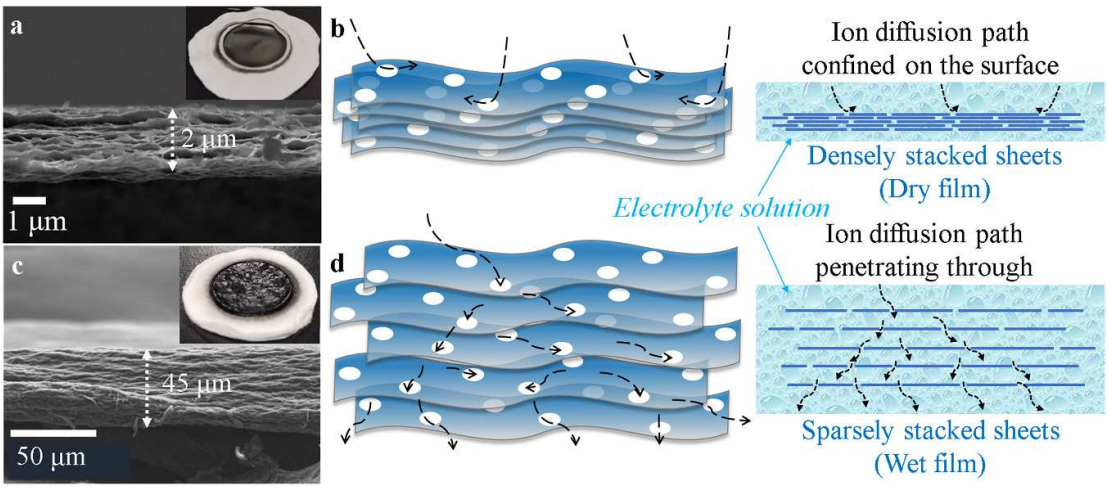

Figure 3. SEM images of cross-section from(a) dry film and (c) wet film. Insets are the photographs of each corresponding sample. Diagrams (perspective view and side view) of (b) densely packing holey graphene film and (d) sparsely packing holey graphene film. The huge difference of interlayer distance results in two totally different ion diffusion behaviors.

interlayer distance between graphene flakes. As water fills the multilayer hG film, the interlayer spacing expands. As a result, the pathways between two adjacent layers will be broadened so that those in-plane nanoholes can link to each other through the pathways and form interconnected ion transport channels. Therefore, ions can travel through the multilayer film faster, which means larger ion diffusion rate in hG wet film, so the electrochemical performance of hG-based supercapacitor is improved. To verify our hypothesis, we use SEM to reveal the cross-sectional morphology of dry film and wet film, then abstract out the images as schematic diagrams, as demonstrated in figure 3.

The SEM images demonstrate the multilayer microstructure of hG film. The dry film (figure 3(a)) has a thickness of 2 μm, while the wet film (figure 3(c)) has a thickness of 45 μm, which is 22 times larger than the former one. This implies a huge difference in interlayer distance inside the multilayer hG film, because both dry film and wet film are prepared from the same amount of hG material and have the same lateral size of 15 mm. The huge thickness difference between dry film and wet film supports our hypothesis, because the wet film has larger interlayer distance to facilitate ion diffusion between two adjacent hG layers. In addition to faster ion diffusion rate, the thick wet film with large interlayer spacing also provides more space to hold ions during charging, thus increasing the capacitance. To visually display the dry film and wet film, the photographs of each are shown as insets. The dry film is thin, smooth and paper-like, while the wet film is thick, rough and sponge-like.

Basing on our hypothesis and the SEM images, we summarize the ion diffusion process in dry film (figure 3(b)) and wet film (figure 3(d)) as schematic diagrams. First of all, residual water in wet film fills the multilayer film as interlayer spacer, expanding the interlayer distance to over 20 times compared to dry film. As a result, in-plane nanoholes and interlayer spacing will have a synergetic effect. While nanoholes generate ion transport channels, expanded interlayer spacing allows those channels to link to each other, forming interconnected channels that can penetrate all the way through the film, therefore accelerating ion diffusion in hG wet film. Without adequate interlayer spacing (figure 3(b)), the ion transport channels will be blocked by densely stacked graphene sheets. Consequently, those nanoholes are isolated and ion diffusion path is generally confined on the surface. In conclusion, we propose the mechanism that is based on the synergetic effect of nanoholes and interlayer spacing. For hG wet film, water acts as spacer, constructs effective ion transport channels, and thus accelerates ion diffusion. This proposed mechanism explains the observed performance improvements and is consist with SEM images.

To further verify our hypothesis, FD hG film was also prepared then characterized by EIS measurements and SEM. The Nyquist plots of hG dry, wet and FD film are shown in figure 4(a). The radius of semicircle for FD film is close to that for wet film while much smaller than that for dry film, which means the charge transfer rate on the interface of FD film is as high as it on the wet film. Similarly, we calculate the ion diffusivity from the slope of linear section. The diffusivity in FD film is 1.34×10^{-11} cm^2 s^{-1}, larger than that in dry film (8.86×10^{-12} cm^2 s^{-1}) but two orders of magnitude smaller than that in wet film (1.33×10^{-9} cm^2 s^{-1}). This result suggests the FD film has intermediate ion diffusion rate among three types of hG film, which implies it has multilayer structure with intermediate interlayer distance.

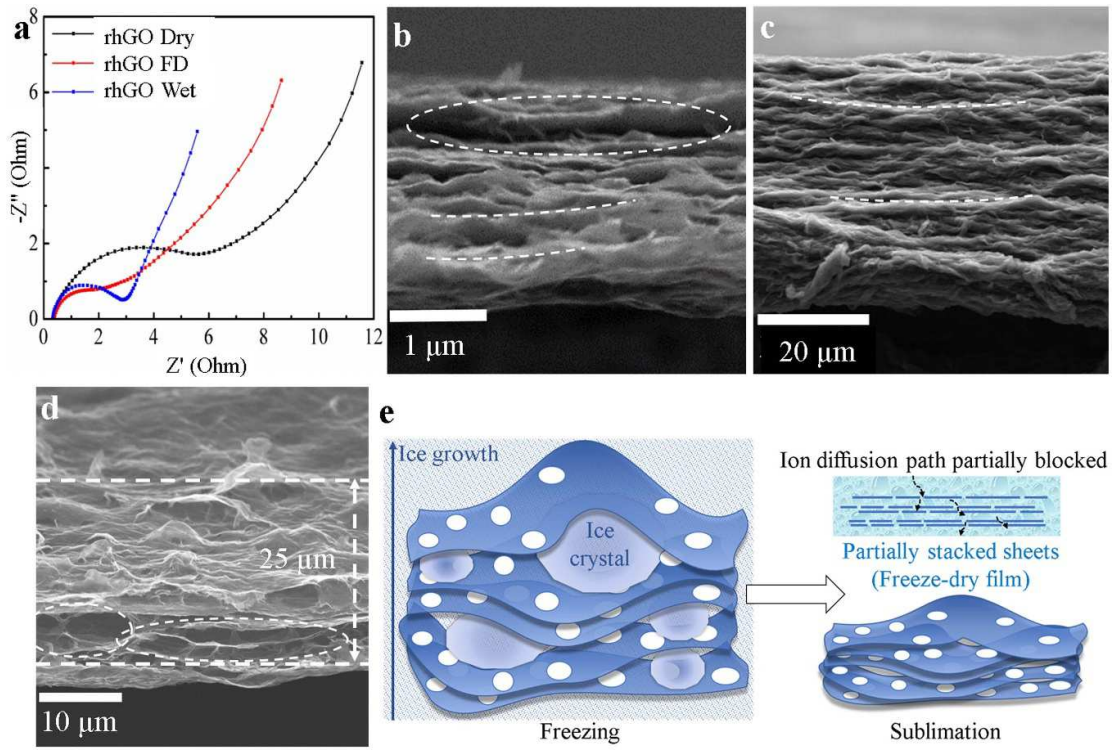

Figure 4. (a) Nyquist plots of holey graphene dry/wet/freeze-dry film. High resolution SEM images of dry (b)/wet (c)/freeze-dry (d) film. (e) The diagrammatic illustration of freeze-drying process and the formation of porous freeze-dry film.

Further observation on cross-sectional SEM images has been conducted to compare the interlayer distance in FD hG film to dry and wet hG films. The high-resolution image of dry film in figure 4(b) displays a large gap among graphene layers and uneven staking of graphene. Nevertheless, no such a gap can be found in wet film (figure 4(c)), and most layers stack parallel to each other evenly. This observation illustrates the effects of residual water, that water fills the multilayer hG film to expand the interlayer spacing and forms more uniform structure, avoiding critical restacking issue during vacuum filtration. For comparison, the cross-sectional SEM image of FD film in figure 4(d) shows the thickness is 25 μm, which is much larger than 2 μm (dry film) but smaller than 45 μm (wet film). This result makes sense because FD film is prepared from wet film through freeze-drying process, during which residual water freezes then sublimates, as illustrated in figure 4(e). The interlayer spacing originally sustained by water will unevenly shrink during freeze-drying. As a result, hG film with intermediate interlayer distance will be formed, meanwhile large pores and uneven stacking will be generated irregularly. In the end, the ion transport channels mentioned earlier will partially be blocked by irregular stacking of graphene. Basing on above Nyquist plots and SEM images, we are able to further verify our hypothesis, that larger interlayer distance can facilitate ion diffusion in hG film and improve hG-based supercapacitor.

We also perform N_2 adsorption and desorption measurements (figure S3) to determine the specific surface area (SSA) of hG dry film and FD film, confirming that FD film has much larger SSA than dry film. This is attributed to less stacking and more porous structure inside FD film (as shown in figure 4), which has larger interlayer spacing over dry film.

3.4. Diffusion model

In addition to the experimental study, we use DFT models to evaluate the effects of interlayer spacing and quantify the relationship between interlayer distance and energy barrier for ion diffusion. We set a symmetrical two-layer configuration of hG, as shown in figures 5(a) and (c). This configuration consists of two layers of hG, and each layer has one nanohole that contains 10 atomic vacancies, with total diameter ranging from 6.29 to 9.88 Å. In this configuration, we consider two modes of movement for a hydrogen ion, that is, hole-to-hole movement (figure 5(a)) and horizontal movement in the middle plane between two layers (figure 5(c)). To quantify the effects of interlayer distance on the energy barrier for diffusion, distances of 7.4 Å, 11.1 Å, and 14.8 Å are studied in each mode.

The energy barrier for hole-to-hole movement under different interlayer distance (figure 5(b)) is calculated by the climbing image method. In this model, a hydrogen ion moves from the initial position

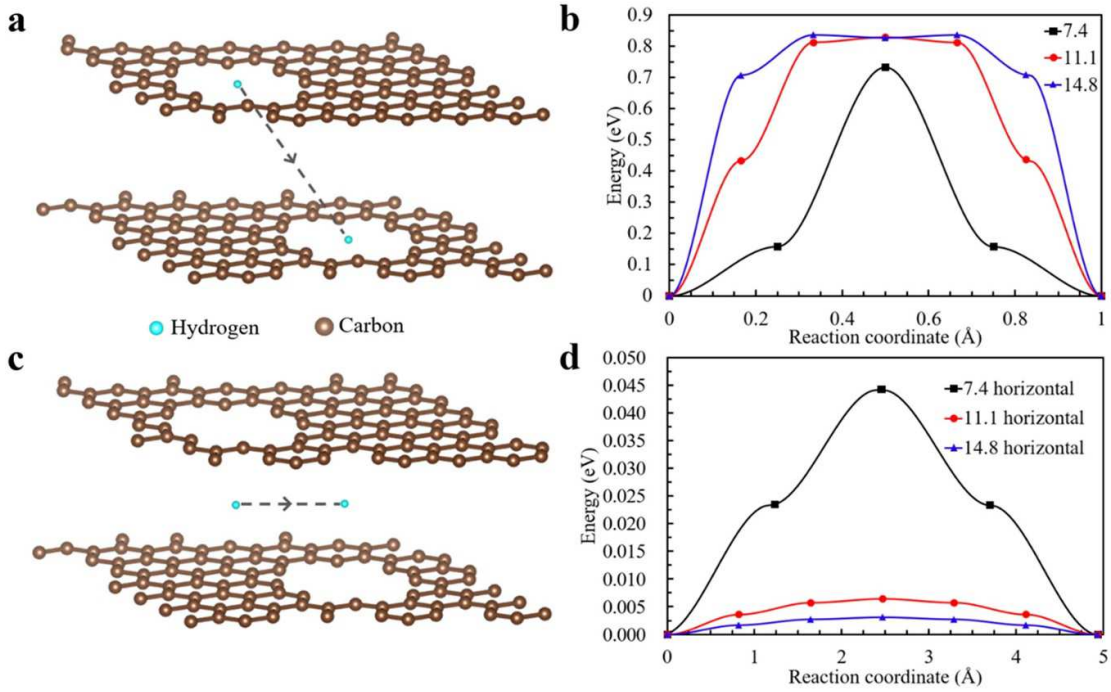

Figure 5. DFT models of ion movement in holey graphene and corresponding energy curves. (a) Hole-to-hole movement of hydrogen ion. (b) Energy barrier for diffusion and minimum energy path of hole-to-hole movement under three different interlayer distance. (c) Horizontal movement of hydrogen ion. (d) Energy barrier for diffusion and minimum energy path of horizontal movement under three different interlayer distance.

where is the center of the first nanohole, toward the final position where is the center of the other nanohole. Since the path length of hole-to-hole movement changes with interlayer distance, the reaction coordinate is normalized for comparison. The three energy curves reveal that the hG configuration with 7.4 Å interlayer distance has the smallest energy barrier of 0.733 eV for ion diffusion. This could be ascribed to the influence of London dispersion forces[52] between graphene and hydrogen ion, which is the weakest intermolecular attraction and applies to the entire space in this configuration. To move from the initial position toward the final position, firstly the hydrogen ion has to overcome the attractive London dispersion forces between itself and the first hG layer. Therefore, along the hole-to-hole path the energy barrier peaks in the middle of two layers due to the symmetry of this configuration, then starts to drop as it approaches the other layer due to increasing attractive force. The energy barrier for the configurations with 11.1 and 14.8 Å interlayer distance is higher (0.827 and 0.828 eV, respectively) because longer hole-to-hole travel path will require more energy for hydrogen ions to overcome the attractive forces from the initial hG layer. In addition, 11.1 Å and 14.8 Å configurations have similar peak energy barrier and flat energy curves in the middle. This could be ascribed to diminishing (even vanishing) of London dispersion forces in the middle regions, so that the hydrogen ion almost moves freely near middle plane. Although we find out that the energy barrier will increase with interlayer distance in the mode of hole-to-hole movement, it could be overcome with the help of external electric field. Forced by appropriate electric field, hydrogen ion can move vertically between two hG layers, so the energy barrier for hole-to-hole movement is not the key factor affecting ion diffusion rate in hG films.

To further understand the ion diffusion process in hG film and figure out how interlayer spacing facilitates ion diffusion, we also study the mode of horizontal movement and calculate the energy barrier using the same hG configurations, as shown in figures 5(c) and (d). The hydrogen ion moves in the middle plane between two hG layers, from the initial position right below the center of the first nanohole, toward the final position right above the center of the other nanohole. Here, we do not normalize the reaction coordinate in horizontal mode since the path length does not change with interlayer distance. As expected, the configuration with 7.4 Å interlayer distance has the largest energy barrier of 0.0442 eV, due to the attraction of London dispersion forces between the hydrogen ion and carbon atoms around the nanohole. However, the energy barrier for the configurations with 11.1 Å and 14.8 Å interlayer distance is one order of magnitude smaller (0.0064 and 0.0030 eV, respectively). Such small energy barrier implies the vanishing of London dispersion forces, resulting in unrestricted horizontal movement in

the middle plane. This agrees with our findings above from the middle region along the hole-to-hole path.

In conclusion, the energy barrier for ion diffusion in the vertical direction increases with interlayer distance, and approaches a maximum value in the middle region between two hG layers. In contrast, the energy barrier in the horizontal direction decreases as the interlayer distance increases, and eventually becomes negligible if the interlayer distance is sufficiently large. However, ions could overcome the first energy barrier by external electric field when charging/discharging the hG film, so the second energy barrier becomes the dominant factor that determines the ion diffusion rate in the film. In the end, our DFT results verify the effects of interlayer spacing and quantitatively prove that large interlayer distance can accelerate ion diffusion in hG film, thus supporting our hypothesis.

4. Conclusion

In conclusion, this research aims at improving the ion diffusion efficiency of microwave-synthesized hG films by tuning the water interlayer spacer towards the improved supercapacitor performance. We prepare hG dry films and wet films by controlling the final stage of vacuum filtration process, resulting in densely packed and sparsely packed films, respectively. Characterizations reveal that the sparsely stacked wet films accommodate 20 times larger interlayer distance compared to the densely stacked dry films. Through electrochemical measurements, the hG wet film demonstrates improved supercapacitor performance with specific capacitance of 239 F g^{-1}, about 82% enhancement over hG dry film of 131 F g^{-1}. Moreover, the wet film displays lower charge transfer resistance and higher ion diffusion rate.

Our DFT modeling rigorously elucidates and highlights the effects of interlayer distance on the energy barrier for ion diffusion. Specifically, the vertical energy barrier increases with interlayer distance, while the horizontal energy barrier decreases. Since ions can overcome the vertical energy barrier by external electric fields, the horizontal energy barrier becomes the dominant factor that determines the ion diffusion rate in the hG film.

Basing on above analysis, we confirm the synergetic effect of nanoholes and interlayer spacing. The residual water within the hG film acts as spacer to construct effective ion transport channels that accelerate ion diffusion. Nevertheless, ion transport channels within the hG film remain inactive if they are blocked due to graphene restacking. A simple strategy like constructing interlayer spacing among hG sheets can make those channels more effective.

Data availability statement

All data that support the findings of this study are included within the article (and any supplementary files). Q7

Acknowledgments

This study is partially supported by NSF Grants CMMI-1826392, CMMI-1825576, and CMMI-1726792. We acknowledge the use of facilities within the Eyring Materials Center at Arizona State University supported in part by NNCI-ECCS-1542160. Q8 Q9

Conflict of interest

There are no conflicts to declare.

ORCID iDs

Kun Bi https://orcid.org/0000-0002-5217-0066
Yan Wang https://orcid.org/0000-0001-9474-6396
Wonmo Kang https://orcid.org/0000-0002-5002-3994
Qiong Nian https://orcid.org/0000-0003-4578-1253

References

[1] Shi S, Xu C, Yang C, Li J, Du H, Li B and Kang F 2013 *Particuology* **11** 371–7 Q10
[2] Farhadi M and Mohammed O A 2015 *IEEE Trans. Ind. Appl.* **51** 3570–8
[3] Lehtimäki S, Li M, Salomaa J, Pörhönen J, Kalanti A, Tuukkanen S, Heljo P, Halonen K and Lupo D 2014 *Int. J. Electr. Power Energy Syst.* **58** 42–46
[4] Rita A A, Misra S, Ahuja R and Oluranti J 2021 Effect of supercapacitor on power supply for rechargeable implanted medical devices *Recent Innovations in Computing* ed P K Singh, Y Singh, M H Kolekar, A K Kar, J K Chhabra and A Sen (Springer) pp 123–34
[5] Pay S and Baghzouz Y 2003 Effectiveness of battery-supercapacitor combination in electric vehicles *2003 IEEE Bologna Power Tech Conf. Proc.* (*23–26 June 2003*) vol 3 p 6
[6] Halper M S and Ellenbogen J C 2006 *The MITRE Corporation, McLean, Virginia, USA* vol 1 Q11
[7] Wang T, Lei J, Wang Y, Pang L, Pan F, Chen K-J and Wang H 2022 *Small* **18** 2203307
[8] Graydon J W, Panjehshahi M and Kirk D W 2014 *J Power Sources* **245** 822–9
[9] Zhang L *et al* 2013 *Sci. Rep.* **3** 1408
[10] Stankovich S, Dikin D A, Dommett G H, Kohlhaas K M, Zimney E J, Stach E A, Piner R D, Nguyen S T and Ruoff R S 2006 *Nature* **442** 282–6
[11] Wang J, Yang S, Guo D, Yu P, Li D, Ye J and Mao L 2009 *Electrochem. Commun.* **11** 1892–5
[12] McAllister M J, Li J-L, Adamson D H, Schniepp H C, Abdala A A, Liu J, Herrera-Alonso M, Milius D L, Car R and Prud'homme R K 2007 *Chem. Mater.* **19** 4396–404
[13] Wang Y, Shi Z, Huang Y, Ma Y, Wang C, Chen M and Chen Y 2009 *J. Phys. Chem.* C **113** 13103–7
[14] Liu C, Yu Z, Neff D, Zhamu A and Jang B Z 2010 *Nano Lett.* **10** 4863–8

[15] Hu Y, Cheng H, Zhao F, Chen N, Jiang L, Feng Z and Qu L 2014 *Nanoscale* **6** 6448–51
[16] Raccichini R, Varzi A, Passerini S and Scrosati B 2015 *Nat. Mater.* **14** 271
[17] Xu Y, Lin Z, Zhong X, Huang X, Weiss N O, Huang Y and Duan X 2014 *Nat. Commun.* **5** 4554
[18] Han X *et al* 2014 *ACS Nano* **8** 8255–65
[19] Xu Y, Chen C-Y, Zhao Z, Lin Z, Lee C, Xu X, Wang C, Huang Y, Shakir M I and Duan X 2015 *Nano Lett.* **15** 4605–10
[20] Zhao X, Hayner C M, Kung M C and Kung H H 2011 *ACS Nano* **5** 8739–49
[21] Jeong J H, Lee G-W, Kim Y H, Choi Y J, Roh K C and Kim K-B 2019 *Chem. Eng. J.* **378** 122126
[22] Chen Z, An X, Dai L and Xu Y *Nano Energy* 2020 **73** 104762
[23] Xu M, Wang X, Li Z, Tan X, Yang M and Zhao J 2023 *J. Alloys Compd.* **938** 168568
[24] Wang D, Dai R, Zhang X, Liu L, Zhuang H, Lu Y, Wang Y, Liao Y and Nian Q 2020 *Carbon* **161** 880–91
[25] Fan Z, Wang Y, Xie Z, Wang D, Yuan Y, Kang H, Su B, Cheng Z and Liu Y 2018 *Adv. Sci.* **5** 1800750
[26] Zang P, Gao S, Dang L, Liu Z and Lei Z 2016 *Electrochim. Acta* **212** 171–8
[27] Zhu Z, Wang Z, Ba Z, Li X, Dong J, Fang Y, Zhang Q and Zhao X 2022 *J. Energy Storage* **47** 103911
[28] Du P, Dong Y, Kang H, Wang Q and Niu J 2019 *Electrochim. Acta* **320** 134610
[29] Zhai S, Wang C, Karahan H E, Wang Y, Chen X, Sui X, Huang Q, Liao X, Wang X and Chen Y 2018 *Small* **14** 1800582
[30] Li D, Müller M B, Gilje S, Kaner R B and Wallace G G 2008 *Nat. Nanotechnol.* **3** 101–5
[31] Kresse G, Furthmüller J and Hafner J 1994 *Phys. Rev.*B **50** 13181
[32] Kresse G and Furthmüller J 1996 *Phys. Rev.* B **54** 11169
[33] Perdew J P, Burke K and Ernzerhof M 1996 *Phys. Rev. Lett.* **77** 3865
[34] Kresse G and Joubert D 1999 *Phys. Rev.* B **59** 1758
[35] Henkelman G, Uberuaga B P and Jónsson H 2000 *J. Chem. Phys.* **113** 9901–4
[36] Grimme S, Antony J, Ehrlich S and Krieg H 2010 *J. Chem. Phys.* **132** 154104
[37] Bi K, Wang D, Dai R, Liu L, Wang Y, Lu Y, Liao Y, Ding L, Zhuang H and Nian Q 2022 *Nanoscale* **14** 4762–9
[38] Estel L, Poux M, Benamara N and Polaert I 2017 *Chem. Eng. Process.* **113** 56–64
[39] Glasnov T N and Kappe C O 2011 *Chem. Eur. J.* **17** 11956–68
[40] Yang F, Xia Y, Tian W, Huang K, Zhang W, Yin S, Yang Y and Zhu H 2023 *Ind. Eng. Chem. Res.* **62** 19459–70
[41] Gao X, Jang J and Nagase S 2010 *J. Phys. Chem.* C **114** 832–42
[42] Malard L M, Pimenta M A, Dresselhaus G and Dresselhaus M S 2009 *Phys. Rep.* **473** 51–87
[43] Chen W, Yan L and Bangal P R 2010 *Carbon* **48** 1146–52
[44] Randles J E B 1947 *Discuss. Faraday Soc.* **1** 11–19
[45] Xu M, Wang X, Li Z, Yang M and Zhao J 2024 *Electrochim. Acta* **473** 143491
[46] Chen W, Abedin M J, Barua T, Mirshekarloo M S, El Meragawi S and Majumder M 2023 *Small* 2304227
[47] Yang Y, Liu Y-X, Deng B-W, Li Y, Yin B and Yang M-B 2023 *Electrochim. Acta* **440** 141751
[48] Wu H, Yuan W, Yuan X and Cheng L 2023 *Carbon Energy* **5** e229
[49] Jiang C, Gao M, Zhang S, Huang L, Yu S, Song Z and Wu Q 2023 *Int. J. Biol. Macromol.* **225** 1437–48
[50] Wang D *et al* 2024 *Nano Today* **55** 102162
[51] Lin Y, Han X, Campbell C J, Kim J W, Zhao B, Luo W, Dai J, Hu L and Connell J W 2015 *Adv. Funct. Mater.* **25** 2920–7
[52] von Lilienfeld O A, Tavernelli I, Rothlisberger U and Sebastiani D 2004 *Phys. Rev. Lett.* **93** 153004